JGR Oceans

RESEARCH ARTICLE
10.1029/2019JC015469

Ocean Bottom Pressure Variability: Can It Be Reliably Modeled?

Alexey Androsov[1,2], Olaf Boebel[1], Jens Schröter[1], Sergey Danilov[1,3,4], Andreas Macrander[5], and Ioana Ivanciu[6]

[1]Alfred Wegener Institute for Polar and Marine Research, Bremerhaven, Germany, [2]Shirshov Institute of Oceanology, Moscow, Russia, [3]A. M. Obukhov Institute of Atmospheric Physics, Moscow, Russia, [4]Department of Mathematics and Logistics, Jacobs University, Bremen, Germany, [5]Marine and Freshwater Research Institute, Reykjavik, Iceland, [6]GEOMAR Helmholtz Centre for Ocean Research Kiel, Kiel, Germany

Abstract Ocean bottom pressure (OBP) variability serves as a proxy of ocean mass variability, the knowledge of which is needed in geophysical applications. The question of how well it can be modeled by the present general ocean circulation models on time scales in excess of 1 day is addressed here by comparing the simulated OBP variability with the observed one. To this end, a new multiyear data set is used, obtained with an array of bottom pressure gauges deployed deeply along a transect across the Southern Ocean. We present a brief description of OBP data and show large-scale correlations over several thousand kilometers at all time scales using daily and monthly averaged data. Annual and semiannual cycles are weak. Close to the Agulhas Retroflection, signals of up to 30 cm equivalent water height are detected. Further south, signals are mostly intermittent and noisy. It is shown that the models simulate consistent patterns of bottom pressure variability on monthly and longer scales except for areas with high mesoscale eddy activity, where high resolution is needed to capture the variability due to eddies. Furthermore, despite good agreement in the amplitude of variability, the in situ and simulated OBP show only modest correlation.

Key Points:
- We analyze the OBP variability as simulated by global ocean models and compare the simulated variability to that measured with PIES
- Ocean models of different numerical formulation and spatial resolution show remarkably similar OBP, except in regions of high variance

Correspondence to:
A. Androsov,
alexey.androsov@awi.de

Citation:
Androsov, A., Boebel, O., Schröter, J., Danilov, S., Macrander, A., & Ivanciu, I. (2020). Ocean bottom pressure variability: Can it be reliably modeled? *Journal of Geophysical Research: Oceans*, *125*, e2019JC015469. https://doi.org/10.1029/2019JC015469

Received 10 JUL 2019
Accepted 16 FEB 2020
Accepted article online 19 FEB 2020

1. Introduction

The interest in ocean bottom pressure (OBP) is largely dictated by two research questions. OBP fluctuations between two ends of a section are related to fluctuations of ocean transport through this section and can be used to monitor large-scale transport variability (Hughes et al., 1999, 2003; Macrander et al., 2010). More importantly, the OBP fluctuations correspond to ocean mass fluctuations, which has bearing on Earth's gravity field (Chambers & Schröter, 2011; Baker-Yeboah et al., 2005; Ponte et al., 2007; Rietbroek et al., 2006; Tapley et al., 2003, 2004). On one hand, since information on Earth's gravity field is provided by satellite missions such as GRACE, the OBP variability simulated by ocean general circulation models can be constrained by the available data providing better state estimates (Köhl et al., 2012), or simply used to learn about the ocean state (Piecuch & Ponte, 2014a, 2014b; Piecuch, 2013, 2015). On the other hand, the OBP variability is of interest to the community dealing with reconstructions of Earth's gravity field (see, e.g., Böning et al., 2008; Brunnabend et al., 2011; Rietbroek et al., 2009), allowing estimates of error covariances over the ocean.

The analysis of GRACE data provided an increasingly refined view on pressure variability at the bottom. However, GRACE is limited in time domain due to mapping interval (<60 days) (Quinn & Ponte, 2011). In addition, Quinn and Ponte (2011) noted that the high-frequency (with periods less than twice the GRACE mapping interval ~30 days) pressure variability at the bottom is underestimated in the Ocean Model for Circulation and Tides, which was used to dealiase pressure variability at the bottom as measured by GRACE. To reduce these smoothing errors, a better understanding of the high-frequency variability of the bottom pressure is required. Since direct OBP measurements are pointwise, general ocean circulation models are invoked to simulate the OBP patterns, or the connection is exploited between the OBP and sea level variability, available from altimetry missions.

The physics of OBP variability is understood relatively well, and numerous studies address its different aspects. In ocean models the ocean dynamics is considered relative to the geoid, and simulated sea level variability corresponds to the variability of dynamic topography, up to the global corrections needed to compensate for the Boussinesq approximation in models and the poorly known hydrological cycle over the

ocean. The change of mass in the vertical column, seen in the OBP fluctuations, comes from contributions due to the change in atmospheric mass, given through fluctuations in the atmospheric sea level pressure, in the dynamic topography and in the mass of fluid column between the unperturbed surface and bottom. The OBP variability is thus tightly connected with sea surface height variability, which is also directly affected by atmospheric loading and hydrological cycle.

The prevalence of barotropic or baroclinic contributions in the OBP variability depends on spatial and temporal scales. Numerical models show that at high latitudes, at a time scale less than or equal to the annual period, circulation is predominantly barotropic, and becomes baroclinic at larger time scales (Bingham & Hughes, 2008; Vinogradova et al., 2007). According to Bingham and Hughes (2008), in ocean shelf regions, OBP changes are mainly determined by changes in barotropic pressure even on time scales longer than seasonal and annual.

Generally, it is assumed that on time scales shorter than monthly the behavior of OBP is largely barotropic, that is, well correlated with the behavior of sea level variability (Bingham & Hughes, 2008; Behnisch et al., 2013; Vinogradova et al., 2007) and hence can be assessed with a barotropic model. However, because of bottom topography and ocean stratification, barotropic motions cause displacements of isopycnals, that is, baroclinic fluctuations. Therefore, baroclinic processes may be locally important even at relatively short time scales (the variability of sea level and OBP is substantially different at seasonal or longer time scales), and the extent to which topography might influence the OBP still poses some questions, in particular, because previous research relies on coarse ocean models, which damp a significant part of simulated internal variability. For example, based on the analysis of an ocean circulation model and in situ sea level, Byrne and McClean (2008) show that in the Agulhas region, steric height dominates the signal of sea level anomaly both at low, less than 20 days, and high periods.

The freshwater fluxes represent the least constrained part of the forcing of global ocean circulation models. First, the measurements of these fluxes over ocean are too sparse to well constrain reanalyses used to force these models. Models, as a result frequently use salinity restoring to partly compensate for this deficiency and to keep them from drifting. Second, the evaporation is computed based on the simulated ocean temperature, so it is biased if the ocean surface temperature is biased, which happens over wide areas, such as upwelling zones. Taken together, these two factors imply that the effect of freshwater fluxes is simulated with large uncertainty. Fortunately, the effect of freshwater fluxes on variability is masked by the effect of atmospheric surface pressure variability (Ponte, 2005).

The atmospheric pressure loading is expected to lead to predominantly barotropic response and is routinely taken into account in barotropic models. It is commonly argued that on time scales of several days the sea level will adjust to the atmospheric pressure so that the effect of atmospheric loading will be nearly compensated (Inverted Barometer effect) in the barotropic response. However, as already mentioned, some baroclinic motions can be generated, and still be seen in the OBP variability.

Despite this general understanding, the question of how well the OBP variability can be simulated with present-day ocean circulation models is far from being solved. Eddy-permitting and eddy-resolving models are expected to simulate strong internal variability, and the question is on the implication for the OBP variations. Furthermore, models have biases, and their results must be compared to observations, to learn what can and what cannot be simulated.

In this paper we analyze the OBP variability simulated by two models, the Finite Element Sea Ice Ocean circulation Model (FESOM) and the Massachusetts Institute of Technology general circulation model (MITgcm) on several meshes to learn about effects of resolution on the simulated OBP variability. We further use a new data set containing records from an array of PIES (Pressure Inverted Echo Sounders) deployed in the Southern Ocean along a transect going from the tip of Africa to the Antarctic, to assess the extent to which in situ variability can be represented by models. This area includes the Agulhas Current and the Antarctic Circumpolar Current characterized by high eddy activity; therefore, the effects of eddies on the OBP variability, if essential, should be visible in these regions. As noted by Kuhlmann et al. (2013), the OBP variability in this region, in addition to the eddy activity pattern, is also related to coastal and topographic features leading to characteristic resonances that can be excited by local wind fields, affecting the turbulence-induced variability of OBP.

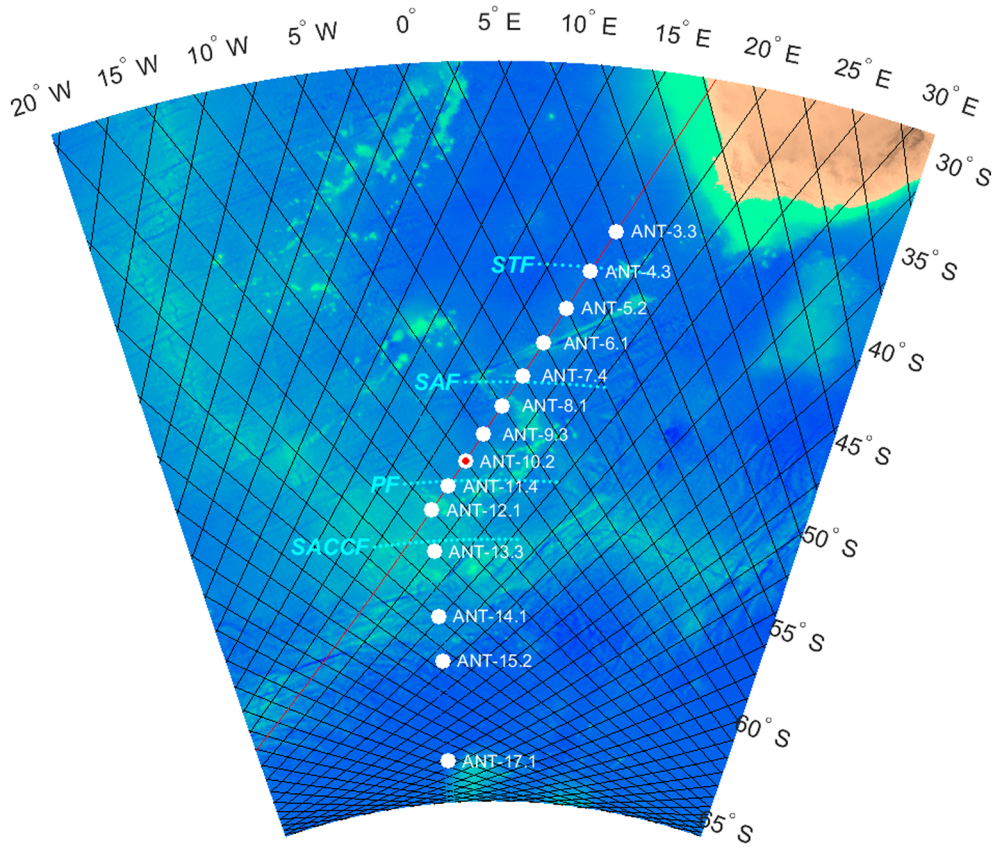

Figure 1. Location of the PIES along the Good Hope section (white dots) including Jason satellite ground tracks (black line, Track 133 marked red) and climatological locations of major ocean fronts (cyan dots).

We begin with the brief description of OBP data set used here (section 2). We continue with the description of models and the analysis of simulated patterns of OBP variability (section 3). Section 4 explores how simulations are related to the observed OBP, and the final section presents the conclusions.

2. A New Long-Term OBP Data Set

PIES deliver bottom pressure, bottom temperature, and travel times of sound signals from the bottom to the sea surface. Over the years, a gradually increasing number of PIES have been deployed by the Alfred Wegener Institute along the Good Hope section south of South Africa (Figure 1). The placement began with two instruments in November 2002 and ended with a -year installment of the full array of 14 instruments deployed from December 2010 through December 2014 (with one exception deployed in December 2011). This study exclusively focuses on this final deployment period with details given in Table A1. The bottom pressure data are named ANT xx.yy with a unique position number xx and a running index yy denoting the temporal mooring index. For easier reading we will call the OBP time series simply ANTxx or PIESxx in most of the following. For the relationship between xx and yy please check Table A1.

2.1. Formal Description

PIES were placed along the Good Hope section between South Africa and Antarctica (Figure 1), which coincides with ground track #133 of the Jason (previously TOPEX/Poseidon) satellite mission to allow direct comparison with altimetry. PIES-to-PIES distances are chosen to resolve the major oceanic fronts of this region.

Most stations are deeper than 4,000 m. The northernmost two positions denoted ANT3 and ANT4 are in the area of the Agulhas Retroflection. Further south the line crosses the mid-ocean ridge, which rises up to 2,600-m depth. The southernmost station ANT17 is already in the dynamically quiet region surrounding the Antarctic continent north of the Antarctic Coastal Current. Practically, the full Antarctic Circumpolar

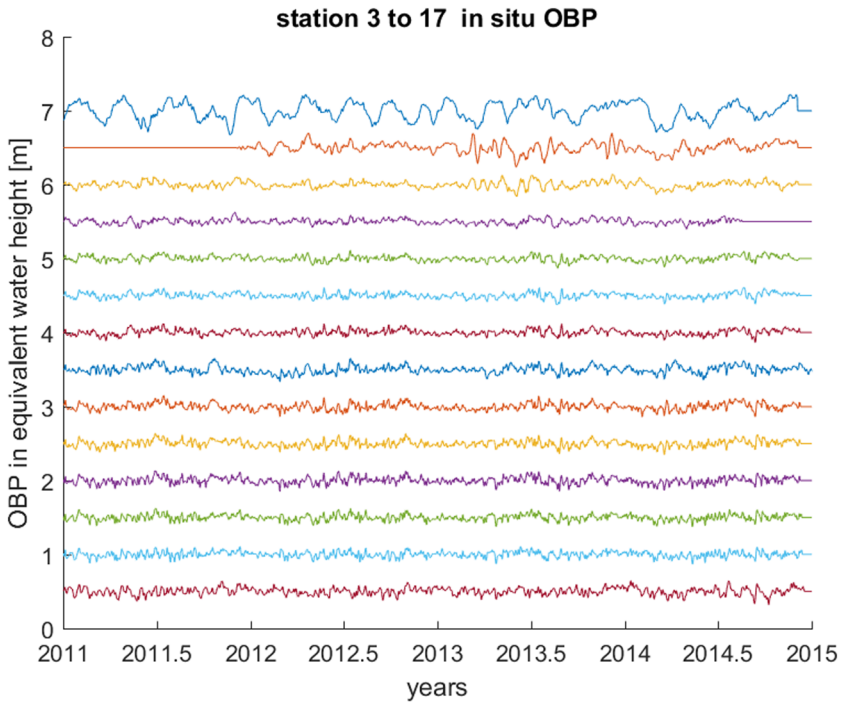

Figure 2. Four years of in situ ocean bottom pressure. The vertical ordering is from North (ANT3, top series) to South (ANT17, bottom series). Values are offset in the vertical by 0.5 m each. Noticeable is the high variance at ANT3 and occasional coherent variations between the stations.

Current and all fronts of the Southern Ocean are sampled by our OBP array. Almost all stations coincide with Topex/POSEIDON crossover points. The PIES were deployed in December 2010, and the full array became operational in January 2011. Most instruments were recovered in December 2014 providing us with a unique set of data. It consists of 14 OBP recordings closely spaced for a period of practically 4 years. ANT10 was recovered a year later and ANT4 was deployed a year later, that is, December 2011. Further technical details can be found in Appendix A.

2.2. Analysis of In Situ OBP

A first impression of the measurements is given in Figure 2. For easier understanding, all pressure values here and below are expressed as equivalent water height (EWH), that is, in meters. Time series are offset vertically by 0.5 m. The data set is close to complete. Missing values are set to undefined and plotted as zeroes. ANT3 and ANT4 exhibit surprisingly large signals when Agulhas variability is present. ANT4 is additionally influenced by motion of the Subtropical Front. Further south all series show fairly low amplitudes.

A closer look reveals annual and semiannual cycles of very low amplitude. They explain only a tiny fraction of the variability observed. Only at ANT3 some of the intermittent signal is projected on the semiannual wave explaining about 9% of the variance, see the relative maxima of the autocorrelation function in Figure 3 at lags of 180 and 360 days. The statistical moments of skewness and kurtosis are close to their expected values of 3 and 0, respectively. Inspection of histograms (not shown) indicates a Gaussian-type behavior. Only ANT3 exhibits a distinctly different behavior. Its probability distribution has a long negative tail with a fat positive tail, apparently connected to Agulhas features.

Let us consider temporal and spatial correlations in our data set. We begin with the autocorrelation depicted in Figure 3, left. A rapid fall off within less than 5 days is visible for time series ANT4 to ANT17. All autocorrelation functions cross the zero line in less than 30 days. ANT3 (depicted with a thick blue line) sticks out with a half width of approximately 14 days and a clear negative lobe at about 42 days and again at 309 days. The fact that for longer time scales the correlation may reach 0.2 leads us to expect some longer-period motion hidden in the intermittent and noisy raw time series. This can be verified by examining the power spectrum (Figure 3, right).

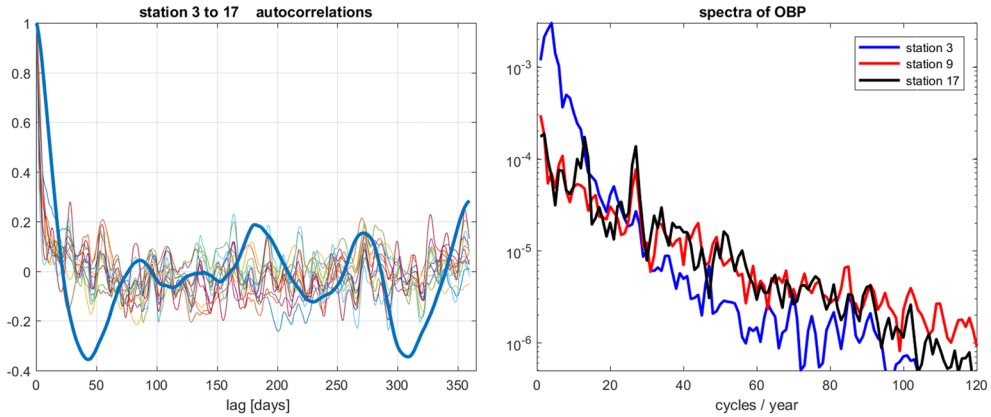

Figure 3. (left) Autocovariance functions of OBP in the Southern Ocean. Only ANT3 in the Agulhas Retroflection (thick blue line) has a decay time of more than a few days. Moreover periods of roughly 3 and 6 months are visible. (right) Spectra of OBP at three representative locations of the Good Hope section. ANT3 in the Agulhas retroflection (blue), ANT9 in the bulk of the ACC (red), and ANT17 in the seasonally ice covered waters close to Antarctica (black). ANT3 exhibits the strongest variations with a maximum at a 4-month period. Relative maxima for ANT9 lie at periods of 52 and 13.5 days. For ANT17 we notice periods of 28 days and again at 13.5 days.

Here, as well as in the results that follow, we find three distinctively different regions. The Agulhas retroflection in the North, the vast region of the ACC, and, finally, a zone with seasonal sea ice cover closer to the Antarctic continent. For simplicity, we will present only three PIES characteristic for their respective dynamic regimes: ANT3, ANT9, and ANT17. A log scale is chosen to visualize the differences in the variances. All spectra are generally red with a more rapid fall off at ANT3. The dominant peak at ANT3 is at four cycles per year. This period is missing at ANT9 and ANT17. Instead, small peaks are visible at seven cycles per year and minor ones at 27 cycles per year, that is, at 13.5 days. Suspicion arises if this could be a result of incomplete removal of tidal signals. At ANT17 a signal sticks out at a period of 28 days.

Following Poropat et al. (2018), we separate the OBP signal into different frequency bands. Periods below 1 day are not considered as they are filtered out already by detiding. Also, we will not distinguish between monthly means and monthly values obtained by filtering with a cutoff of 30 days, as Poropat et al. (2018) show them as difficult to tell apart in practice.

Four bins for periods are taken: (a) below 3 days, (b) between 3 and 10 days, (c) between 10 and 30 days, and, finally, (d) longer than 30 days. Figure 4 shows how the total variance is distributed between the four

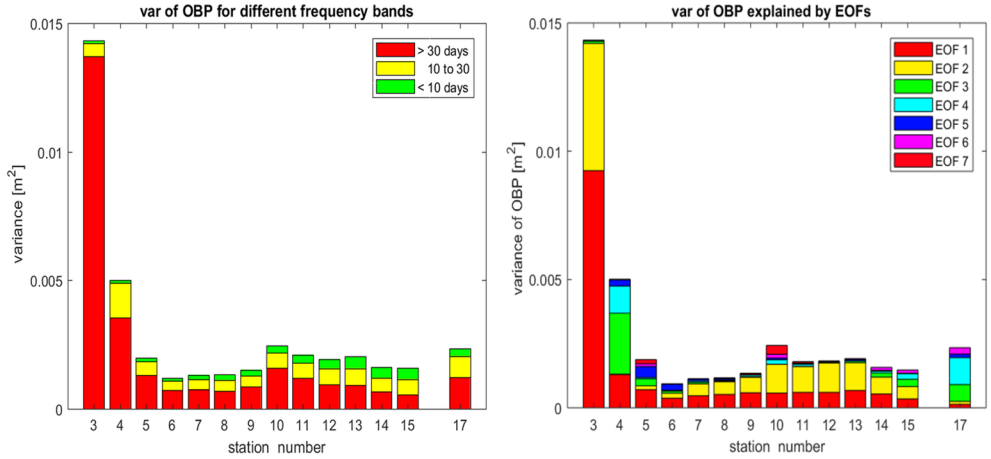

Figure 4. (left) Variance of OBP at the PIES locations, separated into period intervals longer than 30 days (red), 30 to 10 days (yellow), and 10 to 3 days (green). Variance below 3 days is close to nil due to filtering. (right) OBP variance separated into different spatially correlated functions (EOFs). Only the first seven EOFs that explain a cumulative variance of more than 95% are shown. EOF1 explains ANT3 to a large extent and captures a substantial part of the bulk of the ACC. EOF2 describes most of the variance at these locations. EOFs 3 and 4 single out ANT4 and ANT17.

frequency bands. Most prominent is the slow signal at periods greater than 30 days concentrated at ANT3 and ANT4. Faster motion between 10 and 30 days is less pronounced and more evenly distributed. Below 10 days, signals are smaller and growing southward. Finally, we observe very little variance below 3 days.

To explore coherent motion, we performed an expansion in empirical orthogonal functions (EOFs). The OBP matrix is expanded via singular value decomposition: OBP = $\mathbf{USV}^T$ with **U** the matrix of spatial EOFs, **S** the diagonal matrix of singular values, and **V** the time functions or loadings. **U** and **V** are orthonormal basis functions in space and time, respectively. Figure 4 shows how the total variance at the PIES positions is distributed between the EOFs. We note that EOF 1 almost fully explains ANT3 and has little projection on the remainder. EOF 2 describes the bulk of variability in the ACC. EOFs 3 and 4 then describe ANT4 and ANT17, respectively.

We also took a look at the temporal decorrelation of the time functions **V** (not shown). We found that the decorrelation times of the EOF loadings differs from that of the individual PIES. Even the dominant series EOF1 exhibits very short decorrelation times. All loadings decay fast and display fairly high correlations up to 0.4 for longer delay times. However, standard decomposition is distorted as ANT3 and ANT4 dominate the analysis, and they already account for 25% and 20% of the cumulative variance. A way to avoid this would be to normalize the observations by their standard deviations, that is, to work with correlations instead of covariances. Alternatively, the two dominant PIES could be removed by restricting the analysis to ANT5 to ANT17. We chose the second option, as in this case the variances are more balanced. Interestingly, the dominant EOF (30% of remaining variance explained), which describes correlated OBP variations in the ACC has a decay time of only 3 days. These results are not really an improvement over analyzing EOFs of all PIES in conjunction.

An EOF decomposition relies on global correlations. To investigate more local relationships, we study how the OBP at one position can be estimated from all other measurements. To this end we estimate the OBP at one station as a weighted mean:

$$OBP_i = \sum_{j \neq i} w_j OBP_j + \epsilon_i,$$

where the weights w_j are estimated by minimizing ϵ in the least squares sense. It is found that for most PIES large parts of the variability can be expressed in this way. However, for ANT3 and ANT4 as well as for ANT17 outside the ACC the explanation is marginal and amounts to less than 30% of the variance. Inside the ACC more than 70% are explained for fast motions (<3 days), increasing to 80–95% for intermediate motions and somewhat decreasing to 60–80% for periods longer than 30 days. This outcome supports our previous findings of three separate dynamic regimes. In the bulk of the ACC fast and intermediate motions are correlated over large scales, which we will now investigate in more detail.

To this end we consider correlations between the PIES separately at different frequency bands. Cross-correlation matrices are depicted in Figure 5 with latitude versus latitude and a contour interval of 0.2. Let us first look only at the top row of Figure 5, which presents correlations between observed OBP recordings. Beneath we find model results, which are discussed below. The usual four frequency bands and the total signal are shown. We notice only small correlation of ANT3 and ANT4 with the remainder, which emphasizes the unrelated variability of Agulhas system and that of the ACC. Similarly, in the lower left corner of the subplots, ANT17 close to the Antarctic Continent is less correlated to its neighbors at all periods except at 10 to 30 days. The three dynamic regimes of Agulhas Retroflection, ACC, and Antarctic coastal region are again clearly distinguishable.

Although the fast motion at periods smaller than 3 days in Figure 5 is of low amplitude, it is nevertheless highly correlated with space scales in excess of 1,000 km. ANT3 and ANT4 are anticorrelated. Coherent movements cross the Subarctic Front and the Polar Front. Observed length scales of fast motions are shorter than for slower ones.

For the period interval (3 to 10 days) depicted in the next block again high spatial correlations are found. Their length scales increase going south. Only at these periods ANT4 exhibits correlations above 0.6 with its neighbors. At periods between 10 and 30 days ANT3 and ANT4 are independent. Noticeable is the high coherence of ANT14 and ANT15 south of the Southern Antarctic Circumpolar Current Front. For periods longer than 30 days spatial coherence is somewhat smaller. Additionally, we notice a diminished corre-

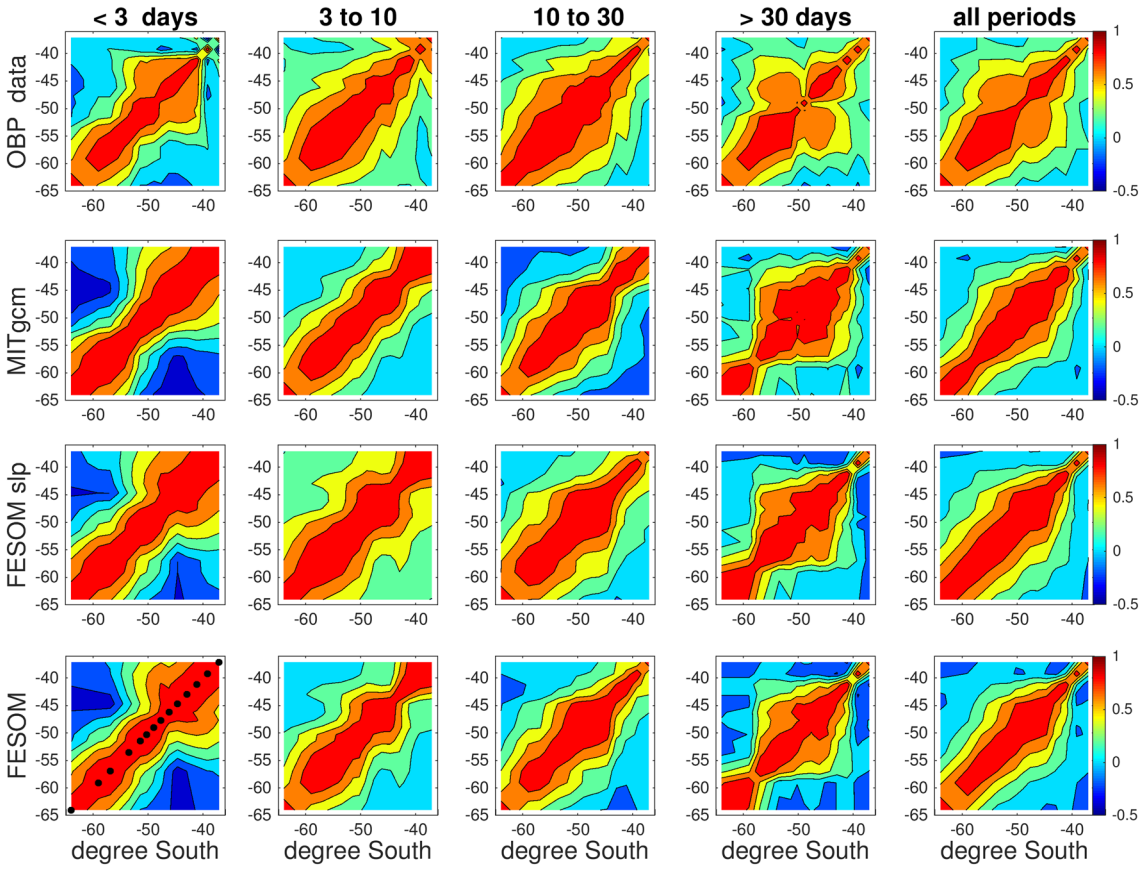

Figure 5. Spatial correlation of OBP at PIES locations (black dots in the bottom left panel). The first row depicts the cross-correlation matrices of the OBP measurements. In the first column motion at periods smaller than 3 days is considered. The next columns present the same matrices for the other frequency bands and finally for the full signal. The rows bellow illustrate the corresponding model output for the MITgcm, FESOM-SLP, and FESOM, respectively. The contour interval is 0.2; axes are latitude versus latitude. Correlation scales inside the ACC are well resolved by observations as well as by modeling. Typically, four stations lie on either side of a PIES before the cross correlation drops below 0.5. Short-period motion (Column 1) shows noticeable shorter spatial correlation in ocean models than in the observations. For the other periods models tend to underestimate correlation radii and may even produce anticorrelations. The longest space scales are found for periods between 3 and 30 days. At ANT10 (near the Polar Front) independent motion is measured for longer periods in addition to the correlated motion at its neighboring stations. This motion is not yet understood, and it is not captured by modeling.

lation at ANT10. Interestingly, OBP north and south of this position has a higher intercorrelation. What causes such a peculiar behavior is not yet understood. Perhaps the Polar Front that usually runs close to the PIES (Figure 1) plays a role in this manner. Spatial correlations for shorter periods are not disturbed at this location. Looking at the total signal including all periods, we obtain a rather similar result, which may be expected as variability above 30 days accounts for more than 50% of OBP variance at most locations.

3. Simulated Patterns of OBP Variability

3.1. A Brief Description of Model Simulations

Model simulations were performed for two periods of time. First, we took available results for the 10-year interval 2000 to 2009 in order to compare global OBP variability. Second, we performed dedicated simulations for the period 2010 to 2014 and try to reconstruct the observed OBP at the PIES positions in the Southern Ocean. In order to study the effect of different model formulations the two established numerical models MITgcm (Marshall et al., 1997) and FESOM (Wang et al., 2014) were used. The impact of horizontal resolution is studied with different meshes, and last but not least the impact of taking atmospheric pressure into account is investigated. In total, eight model runs were considered. They are summarized in Table 1

FESOM is formulated on unstructured meshes and thus allows one to refine the mesh resolution where needed. The FESOM behavior on meshes commonly used in climate modeling (nominal resolution of 1°) is well tuned and documented in the framework of CORE-II intercomparison project (see, e. g., Downes et

Table 1
Summary of the Models

Model	Resolution	Forcing	Loading
Simulation of OBP from 2000 to 2009			
FESOM-15R	15 km	CORE-II	No
FESOM-CORE-II	locally eddy resolving ~10 km	CORE-II	No
FESOM-coarse	1° except Arctic	NCEP	No
MITgcm (ECCO2)	CS510 cubed-sphere 18 km	NCEP	Yes
Simulation of OBP from 2010 to 2014			
FESOM	locally eddy resolving ~10 km	JRA55	No
FESOM-SLP	locally eddy resolving ~10 km	JRA55	Yes
FESOM-coarse	1° except Arctic	NCEP	No
MITgcm (ECCO2)	CS510 cubed-sphere 18 km	NCEP	Yes

al., 2015, and other papers in the same virtual issue). Here we make use of available simulations carried out on several meshes. They include a global mesh with a nearly uniform resolution of 15 km, a mesh that is locally eddy resolving (about 10 km) in the Agulhas region and several other places characterized by high sea level variability (Sein et al., 2016), and a mesh with a coarse nominal resolution of 1° for the entire ocean except for the Arctic region where its spatial resolution is refined to a few kilometers. Simulations on the first two meshes allow us to partly address the effects from permitting or locally resolving eddies. In particular, for the locally refined mesh, Sein et al. (2016) show that the simulated sea level variability in the Agulhas Retroflection region is close to observations.

The other simulations were performed with MITgcm on a 18-km cubed-sphere mesh (CS510). The simulations used were carried out in the framework of the ECCO2 (second phase of the project ECCO—Estimating the Circulation and Climate of the Ocean) program. ECCO2 aims to produce increasingly accurate syntheses of all available global-scale ocean and sea ice data at eddy-resolving scales. It applies a nonlinear free surface formulation and real freshwater flux boundary condition, which provides a more accurate simulation of sea level change (Menemenlis et al., 2008). Although these simulations are only eddy permitting, the simulated ocean state demonstrates sea level variability comparing favorably in amplitude with observations in areas characterized by strong variability. The simulations were run under National Centers for Environmental Prediction (NCEP) forcing with account for atmospheric loading and cover the period from 1992 to 2014.

New model runs were performed to simulate OBP for a direct comparison. To this end, we used FESOM in locally eddy resolving Agulhas setup. Further, instead of forcing the FESOM by the NCEP atmospheric reanalysis (Kalnay, 1996) with daily resolution, we switched to the JRA-55 product (Harada et al., 2016; Kobayashi et al., 2015), which features 3-hourly forcing fields. To quantify the effect of the atmospheric loading, we repeated the simulations in a second (identical twin) model run in which the loading was switched off. These simulations cover the period from 2010 to 2014.

3.2. Modeling the Global Ocean Mean Bottom Pressure

In ocean circulation models the ocean bottom pressure p_b and its global mean can be easily calculated from the hydrostatic approximation:

$$p_b = \int_0^{\zeta} \rho_0 g dz + \int_{-H}^{0} \rho g dz + P_a,$$

where H is the full ocean depth, ζ the dynamic topography, ρ and ρ_0 the density and reference density, respectively, g the acceleration due to gravity, and P_a the atmospheric pressure at the sea level. Obviously, OBP mainly reflects the local depth of the ocean H. However, one should keep in mind that only anomalies are of interest.

Models used in this study are conservative in the sense that there are no internal sources or sinks of volume, heat, or salt. Density change due to steric processes is accounted for. Conserving volume but changing density leads to nonconservation of mass. Nevertheless, Boussinesq models may use a global correction to recover mass conservation (Greatbatch, 1994). After this correction, the global ocean mass is only a function of mass fluxes across its boundaries: precipitation, evaporation, and river runoff ($P - E + R$). The latter

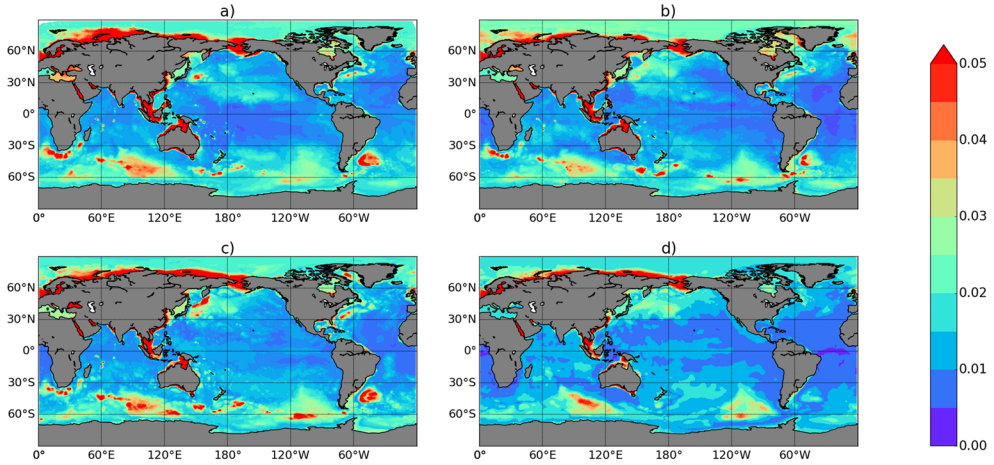

Figure 6. Standard deviation of OBP in meters for the period of simulation 2000–2009 (monthly averages). (a) FESOM-CORE-II; (b) FESOM-15R; (c) MITgcm; (d) FESOM-coarse.

includes fluxes of ground water and inflow of ice grounded on land. Mass fluxes differ spatially and lead to salinity changes. In conjunction with differential heating and cooling they produce buoyancy fluxes at the top of the ocean, which force the thermohaline circulation. The mean OBP can be easily derived from the mean ocean mass by adding the (time-dependent) mean of the atmospheric pressure P_a over the ocean. Changes in gravity or in the shape of the ocean basin are not considered by standard dynamic models.

The hydrological cycle of the ocean is estimated from satellite altimetry giving an annual cycle of roughly 1 cm (Minster et al., 1999) with a trend of 1 to 2 mm/year. On the other hand the global integral of $P - E + R$ observations is the difference of large numbers. Estimates from reanalysis products like NCEP used here are quite noisy and associated with substantial trends of the GMSL of more than 5 mm/year (Schröter et al., 2002). In conclusion it is widely accepted that global mass and global OBP should not be calculated by integration of surface fluxes.

However, when we wish to know the integrals of ocean mass/volume/heat content of the Earth, we are in a good position. International observational programs provide volume (satellite altimetry, TOPEX/Poseidon, continued by the JASON series, ; Fu et al., 2003), ocean mass (started with CHAMP and made useful by GRACE and GRACE-FO, Tapley et al., 2004), or heat content (to a large portion by the autonomous buoy program ARGO, Roemmich et al., 2009).

3.3. Intercomparison of Global Variability

We begin with the simulated variability for the ten year period from 2000 to 2009. The standard deviation of monthly mean OBP anomalies is derived from four numerical simulations over this period. It features high variability at high latitudes (Figure 6) and low variability at mid and low latitudes. The OBP variability on monthly time scales is similar for eddy-resolving/eddy-permitting models (Figures 6a–6c). The FESOM-15R

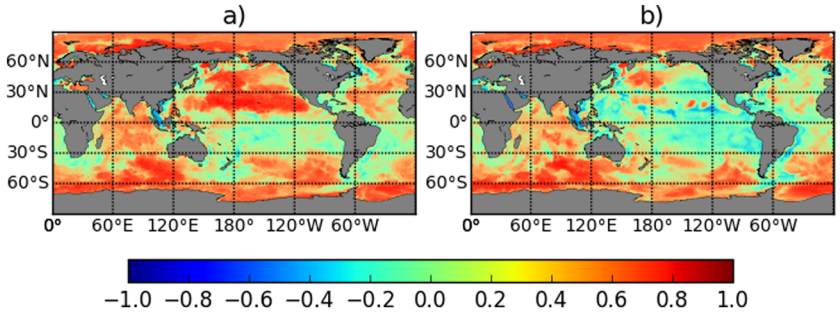

Figure 7. OBP correlation for the period 2000 to 2009 between (a) FESOM-CORE-II and FESOM-15R, and (b) FESOM-CORE-II and FESOM-coarse.

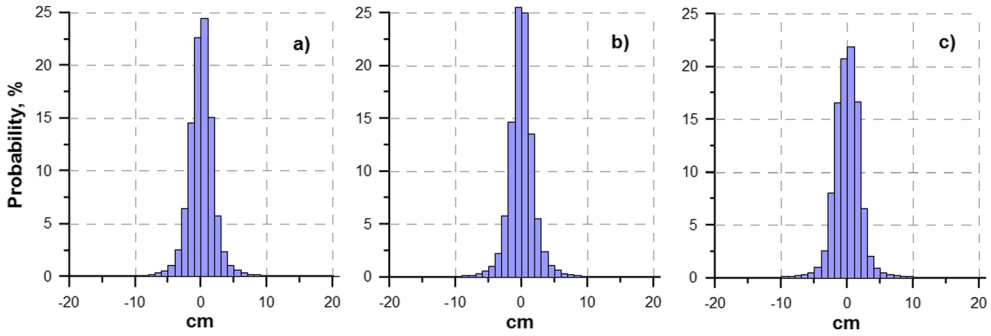

Figure 8. Histograms for the difference in the OBP anomaly between the models: (a) FESOM and FESOM-15R; (b) FESOM and MITgcm; (c) FESOM and FESOM-coarse.

and FESOM-CORE-II runs, where only the spatial resolution is different, lead to remarkably similar patterns (Figures 6a and 6b). Only in the South-East Pacific we notice more variability in the regularly spaced mesh. Also, the MITgcm (Figure 6c) variability is rather alike. In the southern hemisphere signals are a little stronger than at the regular spaced FESOM-15R (Figure 6b) even though the resolution of MITgcm run is slightly worse. Variability simulated on the coarse mesh (Figure 6d) is significantly smaller in zones of enhanced eddy activity and in jet streams.

Looking at the correlations between the different eddy-resolving/eddy-permitting models (Figure 7), we notice high correlations of simulated OBP over large parts of the ocean for models of various spatial resolution. This behavior is likely explained when the main part of OBP variability is given by its barotropic component, which is well represented in model simulations. In regions of high baroclinic motion such as jet streams or the Agulhas retroflection, the flow is turbulent and eddies are simulated with different phases. The result is a lack of coherence, that is, small correlation. When we compare FESOM-CORE-II and FESOM-coarse (Figure 7b), the general picture is the same. However, over large parts of the Pacific Ocean correlation is low or even slightly negative. Seemingly, a lot of variability in the North Pacific is lost (see also Figure 6d). Low correlations in regions of high eddy activity now occur because of the absence of eddies in FESOM-coarse. Over large areas of the Southern Ocean correlations are almost as high as for the higher resolution models.

For a quantitative intercomparison we took the differences in modeled OBP for the 10-year period. As reference we choose the high-resolution FESOM-CORE-II run. Figure 8 shows the three respective histograms of the OBP differences. About 80% of OBP differences lie in the range −2 to 2 cm for eddy-resolving models, reducing to 70% for the difference between the eddy-resolving and coarse model (Figure 8c). These results are rather surprising, given the variety of models investigated. We can confirm that models of various spatial resolutions and forcing reproduce practically the same OBP variability almost in the entire ocean except for frontal zones and zones of high eddy variability.

We now consider the impact of using or neglecting loading by the atmospheric pressure. It is illuminating to consider the loss of root-mean-square (RMS) variability when temporal averaging of 30 days is used instead of 1-day averaging. Thirty-day averaging is commonly performed in the context of the satellite gravity mission GRACE where monthly solutions are standard output. For our area of interest adjacent to the location of the PIES stations Figure 9 presents the results from the FESOM and FESOM-SLP setups for 2011–2014. From the comparison it can be seen that monthly averaging reduces the amplitude of the OBP signal by several centimeters (up to 3 cm). The position of PIES turned out to be not quite representative for this type of investigation. The maxima of differences lie at some distance from the reference stations and there are two pronounced maxima. One is in the region of eddy activity, and the other one is in the middle of the Southern Ocean at the mid-ocean ridge. It is clearly seen that with the account for atmospheric pressure, the differences do not change their structure, but their amplitude changes significantly for the two averaging intervals. Such a structure of differences can be caused by a slightly modified phase of waves propagating in the western direction (Rossby-wave like).

Figure 10 presents the direct assessment of the two model solutions with and without atmospheric loading. It shows the difference in OBP variance (with and without atmospheric pressure) for different time averaging.

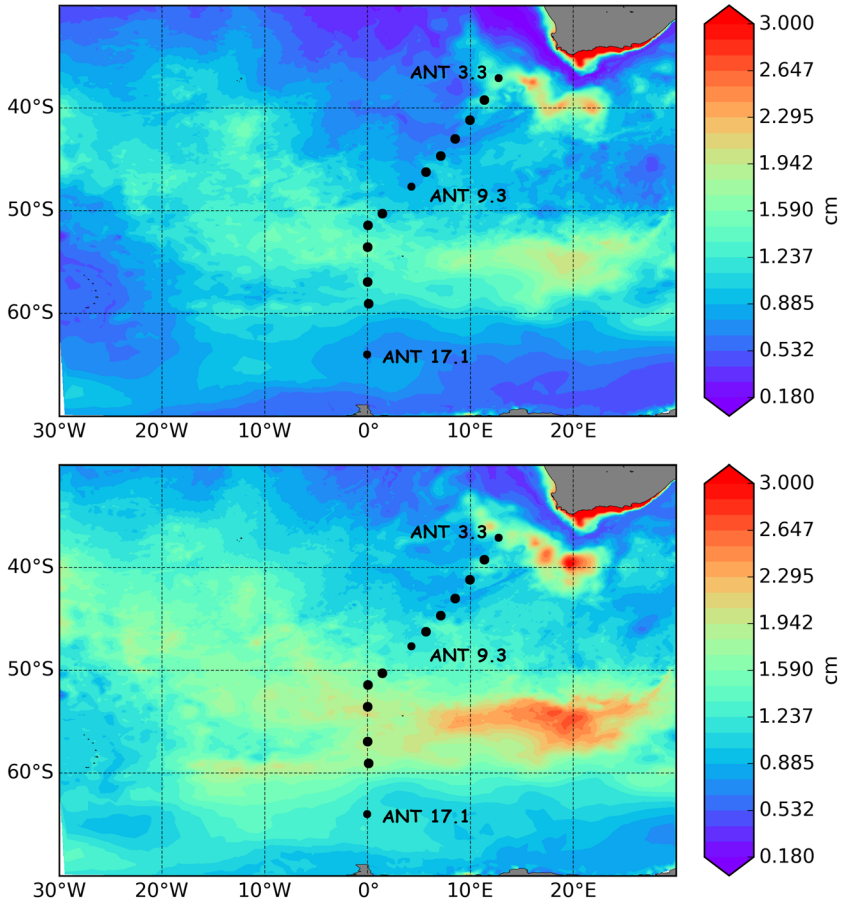

Figure 9. Difference between OBP RMS sampled as 1- and 30-day averages. FESOM simulation for period 2011–2014. (top) FESOM; (bottom) FESOM-SLP.

It can be seen that the local maxima of differences in zones of eddy activity do not change their position or amplitude. Accounting for atmospheric pressure modifies the barotropic waves along the African coast. For 30-day averaging, there are no noticeable differences in the location of the maxima.

4. Comparison of Simulated and Measured OBP Variability

A first evaluation is made in Figure 11. Time series of simulated OBP are shown together with the measurements at four stations. The MITgcm produces eddies in the Agulhas region with roughly correct time scales. However, their amplitude is strongly underestimated and their phases are obviously without relation to nature. At the following stations the agreement of measured and modeled OBP is surprisingly good, especially near the Antarctica. Amplitudes are clearly underestimated but the correlations are quite satisfactory.

In Figure 12 we present a direct comparison of measured and simulated standard deviation for different model versions. The left panel shows the standard deviation when data are averaged with a short window (1 day). The simulated variability is everywhere weaker than observed. The largest OBP variability is measured and modeled at the two stations that are close to the Agulhas Retroflection region. These stations also exhibit the largest differences between the simulated and the observed OBP variability. The 3-hourly forcing used to drive the model is perhaps insufficient to properly excite high-frequency motions. Besides, global ocean circulation models commonly introduce some damping of surface gravity waves, which may be also playing a role here. At all other stations, the standard deviation differs from observations less but still by several centimeters. The simulations show a better agreement to observations if atmospheric pressure loading is accounted for.

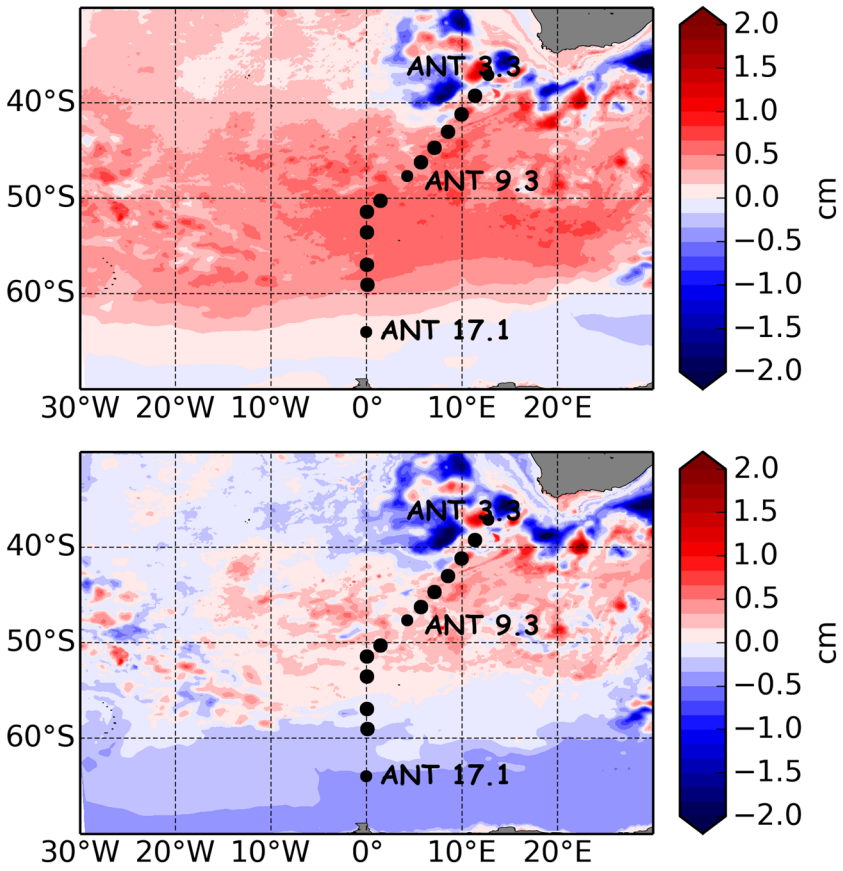

Figure 10. Difference of RMS OBP between simulations with (FESOM-SLP) and without (FESOM) atmospheric pressure loading for the period 2011–2014. The top panel shows 1-day averaging, the bottom panel shows 30-day averaging. Red colors indicate that loading increases variability. Strong signals close to Africa are due to different locations of eddies in the two model realizations.

The right panel of Figure 12 presents computations based on monthly averaging. Here the influence of atmospheric pressure on the OBP variability is smaller, yet the inclusion of atmospheric pressure load improves the result at most locations. This is an expected result, for the atmospheric pressure variability is largely compensated through the Inverted Barometer effect on monthly scales. The observed standard deviation at Station 3.3 is related to the modeled one as 1.26. For the simulations performed with MITgcm the agreement is much worse: the ratio of standard deviations reaches 2.42. However, in the domain of weaker eddy activity FESOM and FESOM-SLP OBP variability agrees slightly less than that of MITgcm. We can explain such difference with lower spatial resolution outside the Agulhas retroflection region.

Figure 13 shows the correlation coefficient between the modeled and observed values. As before, the largest discrepancy falls on the eddy zone in the Agulhas area (Stations 3.3 to 6.1). For stations outside the eddy activity regions, the correlation coefficient is noticeably higher for all sets of experiments with atmospheric pressure. Note that with daily averaging, the correlations computed for MITgcm and FESOM-SLP models, which use the atmospheric pressure forcing, almost coincide. The variability is significantly larger than in simulation without the atmospheric pressure forcing. So, the average correlation coefficient for daily averaging over stations outside the zone of eddy structures of the MITgcm model is at 0.48, while it is slightly higher, at 0.52, for the FESOM-SLP. At the same time, the simulations performed without atmospheric pressure give an average correlation coefficient of only 0.36.

With monthly averaging, the result is changed, see Figure 13, right panel. The simulations with FESOM in runs with and without loading are different, but not as strongly as for daily averaging. The MITgcm simulations show significantly better results. In our opinion, this is due to the fact that with monthly averaging, the contribution of the barotropic signal weakens, and the main contribution comes from the baroclinic part of signal, which the MITgcm manages to simulate closer to reality than the FESOM. Generally, it can be seen

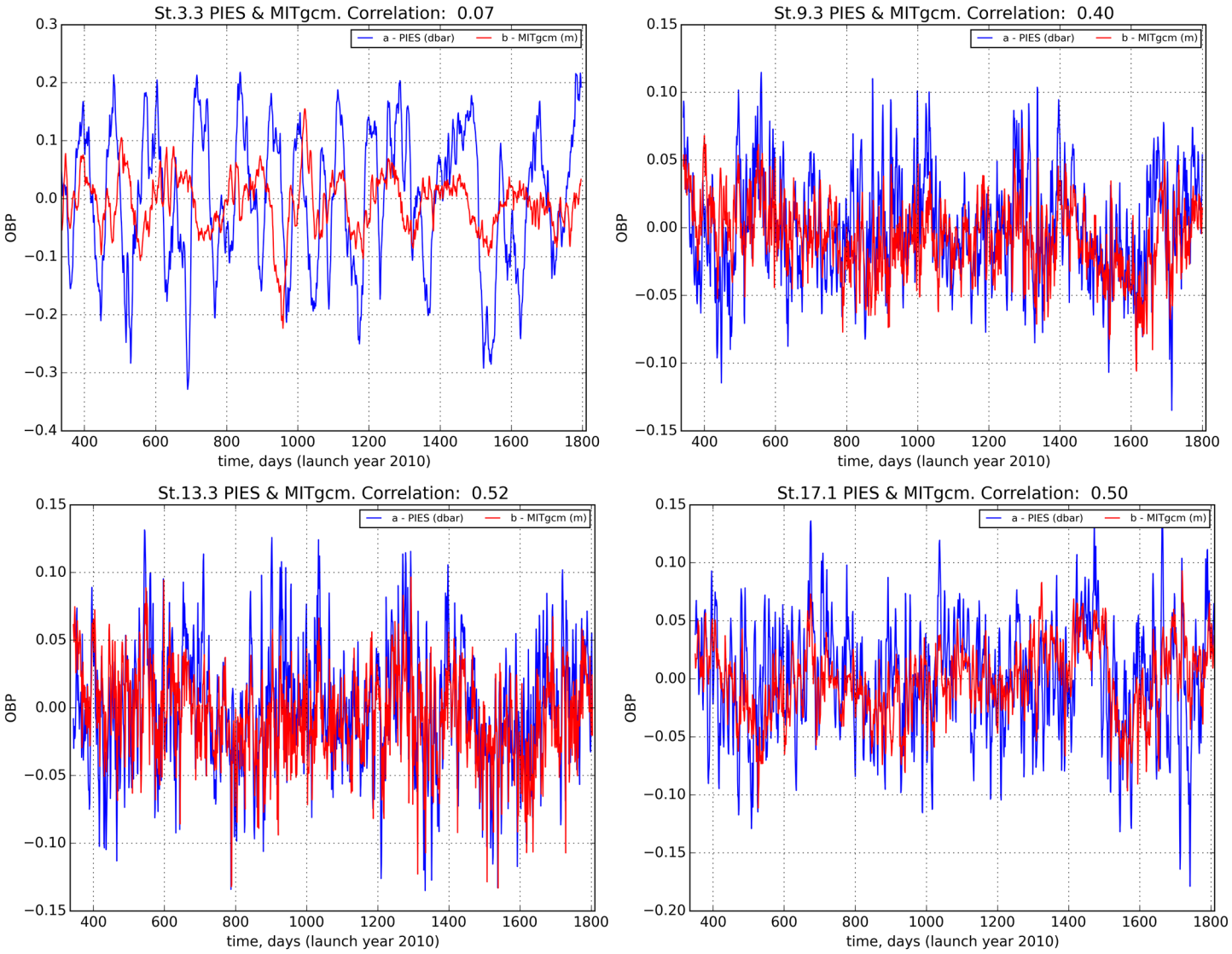

Figure 11. (top left) Measured OBP in meters (blue) and simulated by the MITgcm (red) at Station 3 in the Agulhas region. (top right) Same for Station 9 in the center of the ACC. (bottom left) Station 13 on the bottom of steep slope. (bottom right) Station 17 near the Antarctic coast. Measured variability is underestimated by modeling. Outside the Agulhas retroflection modeled OBP generally follows the observations with correlations of up to 0.5.

that with monthly averaging the model results are somewhat closer to the observational data in simulations run with the atmospheric pressure load.

Figure 14 shows the results of calculating the RMS error for the same experiments as presented above. The overall behavior is not different from the correlation analysis. The greatest errors occur in the zone of strong eddy dynamics. With daily time averaging, the average error at the stations outside the Agulhas region is by 14% smaller in the simulations taking into account the atmospheric pressure load than without it. With monthly averaging, the difference is significantly smaller. It is worth noting that although correlations differ substantially between model runs this is not the case for the RMS error.

Now we will compare spatial correlations simulated by models with those of the observations. The latter have already been presented as the first row in Figure 5. The other rows in Figure 5 display results from the MITgcm, FESOM-SLP, and FESOM, respectively. The most striking feature is the similarity of the three models for periods smaller than 3 days. For longer distances they produce anticorrelations, which contradicts the observations. In models the motions contributing to anticorrelations are seemingly coherent even across the Agulhas Retroflection and also the southernmost part of the Good Hope section. Most of the 3- to 10-day interval can be reproduced quite nicely. Again, model output is very similar and, again, the three

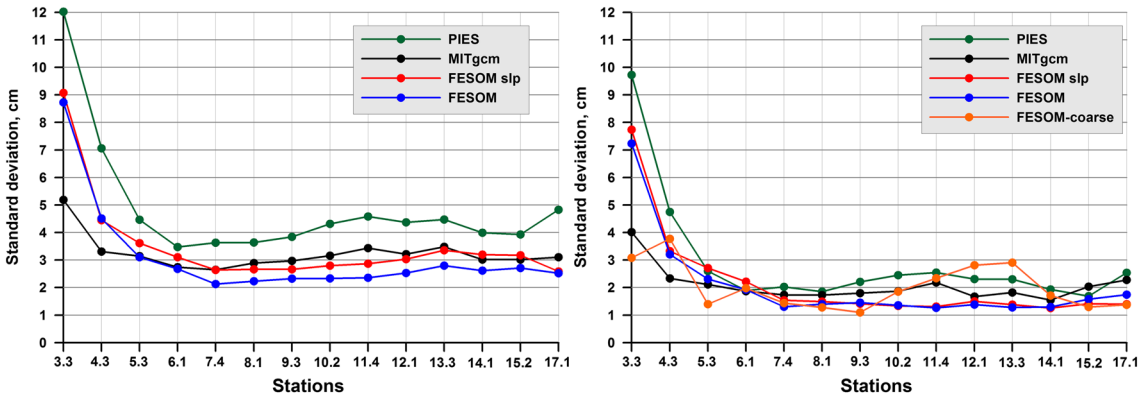

Figure 12. Comparison of OBP standard deviation simulated by MITgcm, FESOM-SLP and FESOM, and FESOM-coarse with PIES for the period December 2010 to December 2014. (left) The standard deviation with 1-day data averaging; (right) the standard deviation with 30-day data averaging.

models miss the break in correlation observed at the Subtropical Front. Continuing with the 10- to 30-day band the MITgcm sticks out. Although it reproduces the general structure well, it features strongly negative long distance correlations, which are not observed. FESOM also produces negative correlations albeit at a smaller level. Best at this frequency range is FESOM-SLP. On monthly time scales all three models capture the separation of dynamics in the region of the Southern Antarctic Circumpolar Current Front. Similarly, all they see the loss of coherence across the Subtropical Front and exhibit slightly higher correlations for the interior. FESOM shows anticorrelations between the three dynamic domains, which are not observed. FESOM-SLP is slightly better in this respect and the MITgcm is best at monthly averages. No model here is able to retrieve the lack of coherence observed at Station 10. Finally, if all periods are combined, model results are fairly good. Models have a tendency toward the extremes with high correlations modeled being too high and low correlations too low or even negative.

In general, one may say that the models used here are able to reproduce low-frequency OBP variability in the sense of total variances. For the high-frequency fraction of variability this is not the case as the models used consistently underestimate variances and correlation length scales. Considering RMS differences to the observed OBP, we find errors as large as the variances themselves. Correlations may reach 0.7 for monthly data and 0.6 for 1-day averaging. Intermodel correlations can be even higher and model to model RMS differences are noticeably smaller than the differences to observations. In summary, the ocean models used here produce similar results but do not sufficiently capture all motions we find in the data.

5. Conclusions and Outlook

A new data set of OBP recordings was used to rigorously test the OBP output of three ocean general circulation models. The data set is unique in the sense that not only variability on time scales from daily to

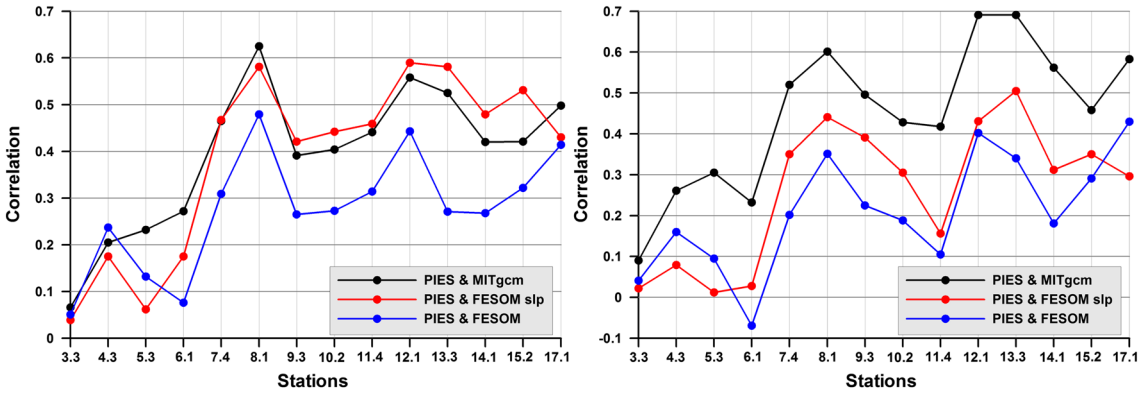

Figure 13. The correlation coefficient between the observed OBP and model simulations for the period from 2011 to 2014. The correlations are computed from daily averages in the left panel and from monthly averages in the right panel.

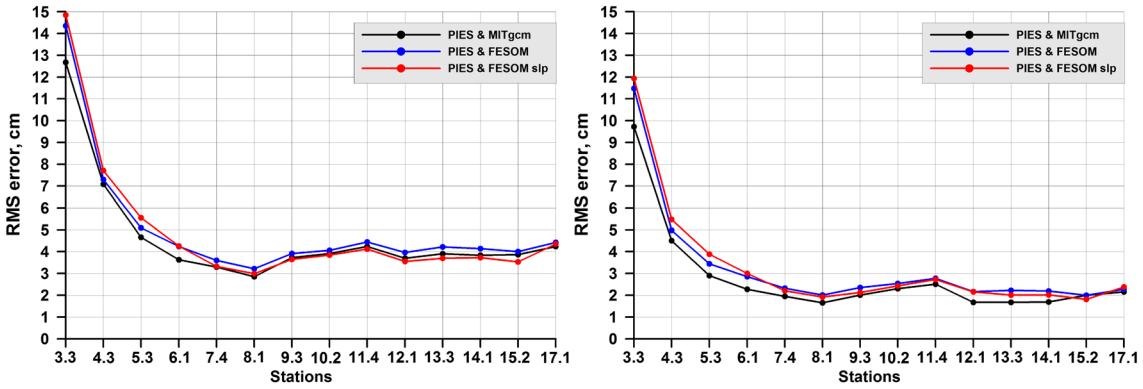

Figure 14. RMS error between OBP observed (PIES) and model for the period from 2011 to 2014. The left panel corresponds to daily averaging, and the right panel corresponds to monthly averaging.

interannual periods can be analyzed. Additionally, horizontal correlations at distances of up to 3,000 km can be evaluated. Due to the experimental setup only detrended anomalies of OBP can be determined and the output of the circulation models needs to be treated in the same manner. Our observed OBP is split into three largely disconnected parts; first, the Agulhas Retroflection Area, a turbulent regime, where OBP variations of up to 30-cm equivalent water height are observed; second, the vast expanse of the Antarctic Circumpolar Current south of the Sub-Antarctic Front showing a more uniform behavior having standard deviation values of 3 to 4 cm; and third, waters seasonally covered by sea ice closer to Antarctica with a value of 5 cm. Annual and semiannual signals are weak and describe less than 5% of the signal variance.

Ocean models considered here generally reproduce these three dynamic regimes with some exceptions. They perform best at periods between 3 and 30 days. At shorter time scales modeled OBP correlations are too large-scale in the Agulhas Retroflection and a little too short-scale further south. On monthly time scales the independence of the Agulhas regime is reproduced while spatial correlations in the southern part of the Good Hope section are underestimated. High-frequency variance is underestimated by all models. Here FESOM with atmospheric pressure forcing gets closest to observed spectra. The high OBP variance at Station 3 can be modeled only with very high model resolution. At a point to point comparison the RMS differences are roughly as large as the signals themselves. However, for some locations correlations can be significant, reaching up to 0.7 for monthly averages. The MITgcm performs best and FESOM without pressure forcing fares worst in this respect.

There is no hope that the phases of OBP variations can be modeled satisfactorily in areas where eddy motion and frontal meandering plays a role. Efforts are underway to use data assimilation in order to mend this model deficit. If successful, there is a chance to improve high-frequency OBP modeling leading to advanced de-aliasing products useful for space gravity missions like GRACE and GRACE-FO.

Appendix A: PIES Dataset

This Appendix contains details about the measuring system and expedition history.

All PIES were firmly seated in steel stands, and deployed free falling. The steel stand ensures a stable position on the ground in support of accurate pressure records. At a distance of 50 m above the PIES, an ET861 Posidonia transponder for underwater localization, and an acoustic current meter (in some cases) for local current measurements were attached via mooring rope. Only one of the 2010 deployments was not successful. At ANT4-2, Posidonia detected the PIES ascending to the surface immediately after hitting the sea floor; it was taken on board and not deployed again in order to reliably solve the apparent mechanical problems of the release. For all following deployments (ANT5 to ANT17), the mooring design was modified ensuring that the PIES release is not overstressed upon impact on the bottom. All except one PIES were recovered during Polarstern expedition ANT29.2 (PS89). In spite of two attempts, PIES at ANT10-ANT2 could not be recovered during this expedition due to foul weather, but it was successfully retrieved 2 years later during Polarstern expedition PS103.

Table A1
Deployment and Recovery of PIES in 2010 to 2014

	Deployment				Recovery			
PIES SN DCS SN Posidonia SN	Mooring ID Station book Deployment CTD	Data time (UTC)	Position (GPS) Depth (DWS)	Final position (best estimate from Posidonia)	Mooring ID Station book Recovery CTD	Release data Release time (UTC)	Position Depth Depth (Posidonia)	Time offset
PIES #058	ANT 3-3	30.11.2010	3705.84'S	3705.80'S	ANT 3-3	04.12.2014	3705.90'S	PIES
no DCS	PS77/013-3	06:31	1245.23'E	1245.48'E	PS89/001-2	07:08	1245.56'E	09:45:12GMT
ET861 #637	PS77/013-1		4904 m	5000 m @07:40	PS89/001-1		4983 m	09:47:20
C-PIES #184	ANT 4-3	05.12.2011	3913.07'S	3913.34'S	ANT 4-3	05.12.2014	3913.67'S	PIES
DCS #752	PS79/035-2	12:07	1120.04'E	1119.98'E	PS89/002-2	01:20	1120.05'E	13:32:48GMT
ET861 #726	PS79/035-3		5122 m	5072 m @13:12	PS89/002-1		5076 m	13:34:00
C-PIES #182	ANT 5-3	02.12.2010	4109.77'S	4109.74'S	ANT 5-3	05.12.2014	4109.87'S	PIES
no DCS	PS77/015-3	08:05	0955.31'E	0955.34'E	PS89/003-2	18:32	0955.61'E	20:47:00GMT
ET861 #469	PS77/015-1		4624 m	4601 m @09:29	PS89/003-1		4605 m	20:48:00
PIES #069	ANT 6-1	02.12.2010	4258.80'S	4258.76'S	ANT 6-1	06.12.2014	4258.46'S	unavailable
no DCS	PS77/016-1	22:17	0830.15'E	0830.00'E	PS89/004-3	11:23	0830.67'E	
ET861 #384	PS77/016-2		3930 m	3871 m @01:00	PS89/004-2		3882 m	
C-PIES #181	ANT 7-4	03.12.2010	4439.73'S	4439.65'S	ANT 7-4	07.12.2014	4439.46'S	PIES
DCS #750	PS77/017-2	18:37	0705.15'E	0705.25'E	PS89/005-2	04:00	0705.60'E	06:18:48GMT
ET861 #639	PS77/017-3		4593 m	4500 m @22:20	PS89/005-1		4540 m	06:18:30
C-PIES #183	ANT 8-1	04.12.2010	4612.97'S	4612.95'S	ANT 8-1	07.12.2014	4612.91'S	PIES
DCS #751	PS77/018-1	14:55	0540.23'E	0540.17'E	PS89/006-2	18:24	0540.51'E	20:28:56GMT
ET861 #616	PS77/018-2		4786 m	4760 m @17:40	PS89/006-1		4767 m	20:29:40
C-PIES #251	ANT 9-3	05.12.2010	4739.87'S	no	ANT 9-3	08.12.2014	4740.34'S	PIES
DCS #26	PS77/019-2	10:20	0415.22'E	reception	PS89/007-2	08:31	0415.03'E	11:12:32GMT
ET861 #602	PS77/019-3		4541 m		PS89/007-1		4504 m	11:17:10
C-PIES #250	ANT 10-2	06.12.2010	4900.77'S	no	ANT 10-2	21.12.2016	4900.74'S	unavailable
DCS #031	PS77/020-2	03:58	0250.05'E	reception	PS103/002-1	14:09	0250.85'E	(depleted
ET861#617	PS77/020-3		4056 m		PS103/002-4		4081 m	batteries)
C-PIES #249	ANT 11-4	07.12.2010	5015.45'S	5015.33'S	ANT 11-4	09.12.2014	5015.40'S	PIES
DCS #24	PS77/021-3	00:13	0125.18'E	0125.00'E	PS89/009-2	15:11	0125.48'E	16:54:01GMT
ET861 #385	PS77/021-2		3901 m	3846 m @01:22	PS89/009-1		3842 m	16:59:00
PIES #062	ANT 12-1	07.12.2010	5125.15'S	5125.23'S	ANT 12-1	10.12.2014	5125.37'S	PIES
no DCS	PS77/022-1	10:52	0000.24'E	0000.42'E	PS89/010-1	01:08	0000.63'E	02:47:03GMT
ET861 #612	PS77/022-2		2713 m	2654 m @11:41	PS89/010-2		2638 m	02:48:10

Table A1
Continued

	Deployment				Recovery			
PIES SN DCS SN Posidonia SN	Mooring ID Station book Deployment CTD	Data time (UTC)	Position (GPS) Depth (DWS)	Final position (best estimate from Posidonia)	Mooring ID Station book Recovery CTD	Release data Release time (UTC)	Position Depth Depth (Posidonia)	Time offset
C-PIES #252	ANT 13-3	08.12.2010	5331.22'S	5331.20'S	ANT 13-1	10.12.2014	5331.35'S	PIES
DCS #32	PS77/026-2	11:23	0000.13'E	0000.23'E	PS89/012-1	18:53	0000.36'E	20:21:12GMT
ET861 #391	PS77/026-3	2642 m	2585 m		PS89/012-2		2570 m	20:26:00
				@12:09				
PIES #191	ANT 14-1	10.12.2010	5655.71'S	5655.60'S	ANT 14-1	12.12.2014	56505.65'S	PIES
no DCS	PS77/034-1	04:15	0000.01'W	0000.10'W	PS89/016-2	08:43	0000.36'E	11:12:51GMT
ET861 #638	PS77/034-2		3673 m	3582 m	PS89/016-1		3714 m	11:15:00
				@06:15				
PIES #189	ANT 15-2	11.12.2010	5902.37'S	5902.39'S	ANT 15-2	13.12.2014	5902.27'S	PIES
no DCS	PS77/042-2	18:51	0005.29'E	0005.52'E	PS89/020-3	11:408	0005.86'E	14:12:52GMT
ET861 #614	PS77/042-2		4647 m	4590 m	PS89/020-2		4594 m	14:14:15
				@20:30				
PIES #125	ANT 17-1	14.12.2010	6400.70'S	no	ANT 17-1	17.12.2014	6400.55'S	PIES
no DCS	PS77/053-1	23:45	0002.72'W	reception	PS89/027-4	12:50	0003.03'E	14:55:02GMT
ET861 #601	PS77/053-2		5201 m		PS89/027-1		5164 m	14:57:00

Data were downloaded from the PIES directly after recovery via RS232 terminal communication and saved to the ship's network drive. Data were processed according to GSO Technical Report No. 2007-02 (Kennelly et al., 2007) using a traditional treatment (see, e.g., Baker-Yeboah et al., 2009). It consists of removing instrumental drift (fast exponential decay and linear trend). This necessary correction very unfortunately also removes the possibility of detecting sea level rise, which would have been a valuable verification for the GRACE mission. Pressure was despiked, detided, and dedrifted. Detiding was performed using the Fortran RESPO.for function provided with the PIES data processing package, based on the work of Munk and Cartwright (1966); see Appendix C Response Analysis of Tides of the URI Inverted Echo Sounder by Kennelly et al. (2007) for details.

All recovered PIES operated flawlessly over the entire deployment period of 3–4 years (see Table A1). Finally, a low-pass filter with width 1 day was applied and the pressure is provided at 12-hr intervals. For a full description of the PIES data processing chain the reader is referred to Watts (1990) and Fields et al. (1991).

Acknowledgments
The project was supported through the project "DFG-SPP1788 Consistent Ocean Mass Time Series from LEO Potential Field Missions" (CONTIM-2). It also received AWI support through Grants AWI_PS89_01 and AWI_PS103_01, and by the state assignment of FASO Russia (Theme 0149-2019-0015). We are indebted to our colleague D. Sidorenko for his support and help with numerous details. We acknowledge the contribution of N. Koldunov for his help in downloading data from MITgcm modeling. We are also very grateful to D. Sein and Q. Wang for providing the setup for further numerical simulation of different resolution FESOM models.

Data Availability Statement

The data used for the analysis reported here, except for the output of MITgcm, can be accessed online (https://doi.org/10.5281/zenodo.3549812). The MITgcm data can be accessed online (http://data.guillaumemaze.org/ecco2-mitgcm). The raw data of PIES observations can be accessed through PANGEA (https://doi.pangaea.de/10.1594/PANGAEA.912236).

References

Baker-Yeboah, S., Watts, D. R., & Byrne, D. A. (2005). Seasonal variation of ocean bottom pressure derived from Gravity Recovery and Climate Experiment (GRACE): Local validation and global patterns. *Journal of Geophysical Research*, *110*, C09001. https://doi.org/10.1029/2004JC002772

Baker-Yeboah, S., Watts, D. R., & Byrne, D. A. (2009). Measurements of sea surface height variability in the eastern South Atlantic from pressure sensor-equipped inverted echo sounders: Baroclinic and barotropic components. *Journal of Atmospheric and Oceanic Technology*, *26*(12), 2593–2609.

Behnisch, M., Macrander, A., Boebel, O., Wolff, J.-O., & Schröter, J. (2013). Barotropic and deep-referenced baroclinic SSH variability derived from Pressure Inverted Echo Sounders (PIES) south of Africa. *Journal of Geophysical Research: Oceans*, *118*, 3046–3058. https://doi.org/10.1002/jgrc.20195

Bingham, R. J., & Hughes, C. W. (2008). The relationship between sea-level and bottom pressure variability in an eddy permitting ocean model. *Geophysical Research Letters*, *35*, L03602. https://doi.org/10.1029/2007GL032662

Böning, C, Timmermann, R., Macrander, A., & Schröter, J. (2008). A pattern-filtering method for the determination of ocean bottom pressure anomalies from grace solutions. *Geophysical Research Letters*, *35*, L18611. https://doi.org/10.1029/2008GL034974

Brunnabend, S.-E., Rietbroek, R., Timmermann, R., Schröter, J., & Kusche, J. (2011). Improving mass redistribution estimates by modeling ocean bottom pressure uncertainties. *Journal of Geophysical Research*, *116*, C08037. https://doi.org/10.1029/2010JC006617

Byrne, D.-A., & McClean, J.-L. (2008). Sea level anomaly signals in the Agulhas current region. *Geophysical Research Letters*, *35*, L13601. https://doi.org/10.1029/2008GL034087

Chambers, D. P., & Schröter, J. (2011). Measuring ocean mass variability from satellite gravimetry. *Journal of Geodynamics*, *52*(5), 333–343.

Downes, S. M., Farneti, R., Uotila, P., Griffies, S. M., Marsland, S. J., Bailey, D., et al. (2015). An assessment of southern ocean water masses and sea ice during 1988–ĂŞ2007 in a suite of interannual Core-II simulations. *Ocean Modelling*, *94*, 67–94.

Fields, E., Tracey, K., & Watts, D. R. (1991). Inverted echo sounder data processing report. *University of Rhode Island GSO Tech. Rept.*, *91*(3), 150.

Fu, L. L., Stammer, D., Leben, R., & Chelton, D. B. (2003). Improved spatial resolution of ocean surface topography from the Topex/Poseidon-Jason-1 tandem altimeter mission. *Eos Transactions American Geophysical Union*, *84*(26), 241–248.

Greatbatch, R. J. (1994). A note on the representation of steric sea level in models that conserve volume rather than mass. *Journal of Geophysical Research*, *99*(C6), 12,767–12,771.

Harada, Y., Kamahori, H., Kobayashi, C., Endo, H., Kobayashi, S., Ota, Y., et al. (2016). The JRA-55 reanalysis: Representation of atmospheric circulation and climate variability. *Journal of the Meteorological Society of Japan. Ser. II*, *94*, 269–302.

Hughes, C., Meredith, M., & Heywood, K. J. (1999). Wind-driven transport fluctuations through drake passade: A southern mode. *Journal of Physical Oceanography*, *29*, 1971–1992.

Hughes, C., Woodworth, P., Meredith, M., Stepanov, V., Whitworth, T., & Pyne, A. (2003). Coherence of antarctic sea levels, Southern Hemisphere annular mode, and flow through drake passage. *Geophysical Research Letters*, *30*(9), 1464.

Kalnay, E. (1996). The NCEP/NCAR 40-year reanalysis project. *Bulletin of the American Meteorological Society*, *77*, 437–471.

Kennelly, M., Tracey, K. L., & Watts, D. R. (2007). Inverted echo sounder data processing manual. Physical Oceanography Technical Reports. Paper 2, 2593–2609.

Kobayashi, S., Ota, Y., Harada, Y., Ebita, A., Moryia, M., Onoda, H., et al. (2015). The JRA-55 reanalysis: General specifications and basic characteristics. *Journal of the Meteorological Society of Japan. Ser. II*, *93*, 53–48.

Köhl, A., Siegismund, F., & Stammer, D. (2012). Impact of assimilating bottom pressure anomalies from GRACE on ocean circulation estimates. *Journal of Geophysical Research*, *117*, C04032. https://doi.org/10.1029/2011JC007623

Kuhlmann, J., Dobslaw, H., Petrick, C., & Thomas, M. (2013). Ocean bottom pressure signals around southern Africa from in situ measurements, satellite data, and modeling. *Journal of Geophysical Research: Oceans*, *118*, 4889–4898. https://doi.org/10.1002/jgrc.20372

Macrander, A., Böning, C., Boebel, O., & Schröter, J. (2010). Validation of grace gravity fields by in-situ data of ocean bottom pressure, in system Earth via geodetic-geophysical space techniques. In F. M. Flechtner, et al. (Eds.), *System Earth via geodetic-geophysical space techniques. Advanced Technologies in Earth Sciences* (pp. 169–186). Berlin, Heidelberg: Springer.

Marshall, J., Adcroft, A., Hill, C., Perelman, L., & Heisey, C. (1997). A finite volume, incompressible Navier-Stokes model for studies of the ocean on parallel computers. *Journal of Geophysical Research*, *102*, 5753–5766.

Menemenlis, D., Campin, J., Heimbach, P., Hill, C., Lee, T., Nguyen, A., et al. (2008). High resolution global ocean and sea ice data synthesis. *Mercator Ocean Quarterly Newsletter*, *31*, 13–21.

Minster, J. F., Cazenave, A., Serafini, Y. V., Mercier, F., Gennero, M. C., & Rogel, P. (1999). Annual cycle in the mean sea level from Topex-Poseidon and ERS-1: Inference on the global hydrological cycle. *Global and Planetary Change*, *20*, 57–66.

Munk, W. H., & Cartwright, D. E. (1966). Tidal spectroscopy and prediction. *Philosophical Transactions of the Royal Society*, *259*, 533–581.

Piecuch, C. G. (2013). Dynamics of satellite-derived interannual ocean bottom pressure variability in the western tropical north pacific. *Journal of Geophysical Research: Oceans*, *118*, 5117–5128. https://doi.org/10.1002/jgrc.20374

Piecuch, C. G. (2015). Vertical structure of ocean pressure variations with application to satellite-gravimetric observations. *Journal of Atmospheric and Oceanic Technology*, *32*, 603–613.

Piecuch, C. G., & Ponte, R. M. (2014a). Nonseasonal mass fluctuations in the midlatitude North Atlantic Ocean. *Geophysical Research Letters*, *41*, 4261–4269. https://doi.org/10.1002/2014GL060248

Piecuch, C. G., & Ponte, R. M. (2014b). Annual cycle in southern tropical Indian Ocean bottom pressure. *Journal of Physical Oceanography*, *44*, 1605–1613.

Ponte, R. M. (2005). Oceanic response to surface loading effects neglected in volume-conserving models. *Journal of Physical Oceanography*, *36*, 426–434.

Ponte, R. M., Quinn, K. J., Wunsch, C., & Heimbach, P. (2007). A comparison of model and GRACE estimates of the large-scale seasonal cycle in ocean bottom pressure. *Geophysical Research Letters*, *34*, L09603. https://doi.org/10.1029/2007GL029599

Poropat, L., Dobslaw, H., Zhang, L., Macrander, A., Boebel, O., & Thomas, M. (2018). Time variations in ocean bottom pressure from a few hours to many years: In situ data, numerical models, and GRACE satellite gravimetry. *Journal of Geophysical Research: Oceans*, *123*, 5612–5623. https://doi.org/10.1029/2018JC014108

Quinn, K.-J., & Ponte, R.-M. (2011). Estimating high frequency ocean bottom pressure variability. *Geophysical Research Letters*, *38*, L08611. https://doi.org/10.1029/2010GL046537

Rietbroek, R., Brunnabend, S.-E., Dahle, C., Kusche, J., Schröter, J., & Timmermann, R. (2009). Changes in total ocean mass derived from GRACE, GPS, and ocean modelling with weekly resolution. *Journal of Geophysical Research*, *114*, C11004. https://doi.org/10.1029/2009JC005449

Rietbroek, R., LeGrand, P., Wouters, B., Lemoine, L.-M., Ramillien, G., & Hughes, C. W. (2006). Comparison of in situ bottom pressure data with GRACE gravimetry in the Crozet-Kerguelen region. *Geophysical Research Letters*, *33*, L21601. https://doi.org/10.1029/2006GL027452

Roemmich, D., Johnson, G. C., Riser, S., & Ignaszewski, M. (2009). The Argo program observing the global ocean with profiling floats. *Oceanography (Washington D.C.)*, *22*(2), 34–43.

Schröter, J., Wenzel, M., Staneva, J., Reick, C., & Danilov, S. (2002). What are the sources of sea level rise?—Results from a 50 year hindcast with a global OGCM. Jason-1 Science Working Team, Biarritz 2002 meeting.

Sein, D. V., Danilov, S., Biastoch, A., Durgadoo, J. V., Sidorenko, D., Harig, S., & Wang, Q. (2016). Designing variable ocean model resolution based on the observed ocean variability. *Journal of Advances in Modeling Earth Systems*, *8*, 9043–916. https://doi.org/10.1002/2016MS000650

Tapley, B. D., Bettadpur, S., Watkins, M., & Reigber, C. (2004). The gravity recovery and climate experiment: Mission overview and early results. *Geophysical Research Letters*, *31*, L09607. https://doi.org/10.1029/2004GL019920

Tapley, B. D., Chambers, D. P., Bettadpur, S., & Ries, J. C. (2003). Large scale ocean circulation from the GRACE GGM01 geoid. *Geophysical Research Letters*, *30*(22), 2163.

Vinogradova, N. T., Ponte, R. M., & Stammer, D. (2007). Relation between sea level and bottom pressure and the vertical dependence of oceanic variability. *Geophysical Research Letters*, *34*, L03608. https://doi.org/10.1029/2006GL028588

Wang, Q., Danilov, S., Sidorenko, D., Timmermann, R., Wekerle, C., Wang, X., et al. (2014). The Finite Element Sea Ice-Ocean Model (FESOM) v.1.4: Formulation of an ocean general circulation model. *Geoscientific Model Development*, *7*, 663–693.

Watts, D. R. (1990). Deep-ocean bottom pressure measurements: Drift removal and performance. *Journal of Atmospheric and Oceanic Technology*, *7*, 296–306.